AIAA at 50

Anniversary Celebration

AIAA-81-1265 Finite Volume Solution for the Euler Equation for Transonic Flow over Airfoils and Wings Including Viscous Effects

W. Schmidt, Dornier GmbH,
D-7990 Friedrichshafen, FRG

A. Jameson, Princeton University,
Princeton, NJ

D. Whitfield, Mississippi State
University, State College, MS

AIAA 14th Fluid and Plasma Dynamics Conference

June 23-25, 1981/Palo Alto, California

FINITE VOLUME SOLUTIONS FOR THE EULER EQUATIONS FOR TRANSONIC FLOW OVER AIRFOILS AND WINGS INCLUDING VISCOUS EFFECTS+

Wolfgang Schmidt
Theoretical Aerodynamics Department
Dornier GmbH, Postfach 1420
D-7990 Friedrichshafen, Germany

and

Antony Jameson, Professor
Department of Mechanical and Aerospace Engineering
Princeton University
Princeton, NJ 08544

and

David Whitfield, Professor
Department of Aerospace Engineering
Mississippi State University
Mississippi State, MS 39762

Abstract

An efficient numerical method for solution of the two- and threedimensional transonic Euler equations has been used to compute the flow over airfoils, wings and wing-body combinations. For two-dimensional flow the Euler equation code has been coupled with an inverse boundary layer integral method to compute viscous flow over transonic airfoils with shocks. All Euler methods are using the same mesh systems (O- or C-Type) as well established full potential codes which can optionally also provide initial solutions. This allows for detailed comparisons with the full potential solutions. Results are discussed in detail for lifting and nonlifting airfoils as well as the DFVLR-F4 transonic transport configuration.

+ This work was partially supported by the Ministries of Defense and Research and Technology of the Federal Republic of Germany

I. Introduction

While potential flow solutions have proved extremely useful for predicting transonic two- and threedimensional flows with shocks of moderate strength, e.g. see Ref. 1-3 typical of cruising flight of transport and some class of fighter aircraft, the approximation of ignoring entropy changes and vorticity production cannot be expected to give acceptable accuracy when the flight speed is increased into the upper transonic range. More important, however, than the change in pressure rise for a shock as pointed out by Lock[4] seem to be the effects on lifting flows due to the assumptions inherent to the Kutta condition in potential flow theory. One part of this paper will study this effect in detail.

Methods available for simulating transonic viscous flow over airfoils are either Navier-Stokes methods, e.g. Ref. 5, or inviscid methods coupled with boundary-layer solutions. Whereas the Navier Stokes equations properly describe interacting flows, these equations are presently restricted

from routine use because of computer requirements and lack in physical understanding. Inviscid flow boundary layer coupling methods on the other hand require less computer resources, but these methods have been developed for irrotational inviscid flow and usually attached boundary layers, see Ref. 4, 6, 7. In the present paper the Euler equation solver allowing for rotational inviscid flow is coupled with an inverse integral boundary layer method to allow for attached or separated boundary layers, thus avoiding problems in dealing with strong shocks as reported by Lock[4].

The third part of the paper deals with three-dimensional wing and wing-body flow. Presently only potential flow solvers are in use based on the TSP or full potential solution. Ref. 8 presents an interesting review comparing different methods with experimental data. However, all methods exhibit the need for an added vortex sheet as disconuity surface. Since the introduced jumps in potential are confined to be constant along y = const lines rather than streamlines, those methods exhibit wrong physical models near the wing tip or for small aspect ratio wings. These problems can be overcome by solving the full Euler equations in conservation form since this will capture discontinuities and no vortex sheets have to be added explicitly.

Based on previous experiences on airfoil, inlet and wing computations the finite volume approach as introduced by MacCormack[9] has been chosen. Recent efforts, however, to improve the efficiency have led to a new multi-stage, two-level scheme which is described in detail in an other paper of the present conference[10]. The Euler codes based on these schemes operate on O- or C-meshes provided by existing full potential solvers. Since the same mesh is being used, this allows for direct comparisons between full potential and Euler solution, moreover, the full potential solution can be used as starting solution for the Euler solver.

Presently, the methods have been applied to lifting and nonlifting airfoils, cascades, wings, wing-body combinations and inlets. In the present paper detailed comparisons are given for lifting and nonlifting airfoils as well as the DFVLR-F4 wing-body combination which is a standard test case in GARTEur AG01. Special attention is given the effect of separation in inviscid compressible flow as studied on the circular cylinder. Most cases have been run on an IBM 3031, the codes, however have also been tested on CDC 6600, CYBER 203 and CRAY 1 machines.

II. Euler Equation Method

The numerical method used to solve the time-dependent Euler equations is described in detail in Ref. 10. The version used in all airfoil cases and for the wing-body configuration is the unsplit three-stage two-level scheme with total enthalpy constant and local time step. The Courant number is always set equal to two. The basic time stepping scheme is followed by a filter at each time step which introduces an effective artificial viscosity. Only for the present cylinder flow solutions the four-stage two-level scheme with an enthalpy-forcing term and the additional dissipative term as described in Ref. 10 has been used to guarantee highly converged and accurate solutions. The far field boundary conditions are non-reflecting and allow either for sub- or supersonic free stream Mach numbers. All solid surfaces have no flux boundary conditions, the wall pressure being extrapolated from the field. For viscous simulations the flux through the wall is given by the source velocity equivalent to the boundary layer displacement thickness.

III. Inverse Boundary Layer Method

The singularity associated with boundary-layer computations at separation is avoided by using an inverse boundary-layer calculation method. By specifying, for example, the displacement thickness distribution instead of the pressure distribution (a so-called inverse method) this singularity is removed[11] and boundary-layer computations can proceed throughout separated regions. The inverse method used here is the mean-flow kinetic energy integral method described in Ref. 12. This method is based on turbulent boundary-layer velocity profiles that describe separated or attached flow. The same calculation scheme

is used whether the flow is attached or separated and hence no switching or artificial fix is required for points near separation. The dissipation integral is evaluated at each streamwise location using the velocity profiles and the Cebeci-Smith algebraic eddy viscosity model.

In an inverse boundary-layer method, pressure is a dependent variable, and in the particular inverse method used here the displacement thickness (δ^*) distribution is specified. The method used to provide a rational, a priori, specification of the δ^* distribution is the method of Carter[13]. Carter's method can be written as

$$\delta^{*(m+1)} = \delta^{*(m)} + \omega\delta^{*(m)} \left(\frac{u_{e,v}}{|\vec{q}|_{w,i}} - 1\right) \qquad (1)$$

where $\delta^{*(m+1)}$ is the new displacement thickness at a streamwise location, $\delta^{*(m)}$ is the displacement thickness from the previous iteration, $u_{e,v}$ is the local velocity at the edge of the boundary layer obtained from the last boundary-layer solution, $|\vec{q}|_{w,i}$ is the magnitude of the local velocity vector obtained from the last Euler equation solution, and ω is the relaxation parameter.

Figure 1 illustrates that Eq. (1) can also be used with an inverse method to solve a conventional attached flow boundary-layer problem (albeit an increasingly adverse pressure gradient flow) with known pressure distribution. For such a problem, the known pressure distribution is used to determine the velocity distribution which corresponds to $|\vec{q}|_{w,i}$ in Eq. (1). In this case the term $|\vec{q}|_{w,i}$ would, of course, remain fixed at each streamwise location and Eq. (1), with $u_{e,v}$ updated after each inverse boundary-layer solution, is used to obtain the converged δ^* distribution. Figure 1 illustrates that the inverse method, with Eq. (1) used for updating δ^*, provides essentially the same result as the direct method after about 4 iterations with $\omega = 2$ and the initial δ^* distribution being that for a flat plate. Therefore, although a direct method is faster than an inverse method for attached flow because iteration is not required, a direct method is not required.

IV. Viscid-Inviscid Coupling

The method used to achieve viscid-inviscid coupling is the surface source model (or the method of equivalent sources of Lighthill[14]). This method has an advantage over the effective displacement surface approach in that a surface source mass flux is imposed as a boundary condition in the inviscid calculation at the physical body surface or in the wake, and hence mesh adjustment during the iteration process is not required. The surface source mass flux, $(\rho v)_n$, imposed at the physical surface is given by

$$(\rho v)_n = \frac{d(\rho_e u_e \delta^*)}{dx} \qquad (2)$$

where $(\rho v)_n$ is the local mass flux normal to the surface. The right hand side of Eq. (2) is evaluated after each inverse boundary-layer solution to determine $(\rho v)_n$ for subsequent inviscid calculations.

The viscid-inviscid interaction calculation scheme proceeds in the following steps.

1. The Euler equation solutions is advanced 20 to 50 cycles with $(\rho v)_n \equiv 0$.

2. An inverse boundary-layer solution is obtained with $\delta^{*(1)}$ given by Eq. (1), where $\delta^{*(0)}$ is a flat plate distribution, $u_{e,v}$ is constant at the free-stream value (u_∞), and $|\vec{q}|_{w,i}$ is obtained from the last cycle of the Euler equation solution.

3. The Euler equation solution is advanced 20 to 50 cycles with $(\rho v)_n$ held fixed at the value given by Eq. (2).

4. An inverse boundary-layer solutions is obtained with $\delta^{*(m+1)}$ given by Eq. (1).

5. Steps 3 and 4 are repeated until convergence on δ^* or c_p (surface pressure coefficient) is obtained.

The number of cycles the Euler equation solution is advanced in steps 1 and 3 depends upon the problem. For example, if strong shocks form in the early cycles of the Euler equation solution and if over relaxation is used, like $\omega = 2$, it can

be advantageous to call the inverse boundary-layer solution after only a few cycles. It is possible to obtain a converged viscid-inviscid interaction solution in fewer cycles than required to obtain a converged inviscid solution due to a weaker shock resulting from the inclusion of viscous effects. However, most solutions presented were cycled 1.5 to 2 times the number of cycles required for a purely inviscid solution.

V. Mesh Generation

Two- and three-dimensional contour-conformal grids are constructed using standard O- or C-type procedures. Since the mesh generation has been separated from the Euler solver, any mesh can be used, as long as the O or C-logics are not violated, because they will influence the lines or surfaces where boundary conditions have to be provided. In the present paper parabolic coordinates are used as C-type mesh and a mapping to a near circle as O-tpye mesh. For three-dimensional wings parabolic coordinates are used in constant spanwise stations while for arbitrary wingbody combinations a Thompson-type mesh generator has been adapted based on the concept of Yu[15].

Standard meshes for two-dimensional studies have been 128x32 for the O-type and 121x30 for the C-type. Special attention has been given to the O-type mesh since it allows for a very dense spacing at the trailing edge, thus allowing studies of the trailing edge behaviour. For viscous flows, however, the C-type mesh seems to be favourable since it allows for a dense spacing of the wake region. The mesh at the trailing edge and the near wake is almost, resp. easily can be, adjusted to the streamlines, which will provide a good capturing of discontinuities.

Standard meshes for three-dimensional studies up to now have been 40x8x8 and 80x16x16, since the whole computation is being done in core. Standard mesh for runs on the CRAY will be 120x24x24.

Mesh refinement techniques can easily be adapted, however have not been used in the present study because of the use of full potential methods to provide starting solutions.

VI. Kutta Condition

In two-dimensional lifting inviscid isentropic flows a Kutta condition has to be specified at the trailing edge which generally is implemented in computational methods as static pressure to be equal at both upper and lower surface trailing edge. Since in potential flow total pressure is constant everywhere this condition will force the total velocity on both sides to be zero for non zero trailing edge angle and equal and finite for zero-trailing edge angle.

In rotational flow, e.g. transonic flow with a shock on the upper surface, the total pressure behind the shock on the upper surface is smaller than on the lower surface corresponding point, thus forcing a difference in total velocity for constant static pressure. This enforces the inviscid flow to leave at the trailing edge and to be single valued since no solution with $|\vec{q}| \neq 0$ on the smooth upper or lower surface is possible. The only possible solution is the one depicted on Fig. 2 where the flow will leave the surface with the higher total pressure smoothly and a slip line is formed. In compressible flows without shocks again only the one solution with $|\vec{q}| = 0$ at the trailing edge and a flow leaving in the bisector direction is possible. This is due to the fact that any flow around the trailing edge would cause expansion to $M \to \infty$ which has to be terminated by a shock if the flow will leave the upper surface (Fig. 2). Again, this would cause two different tangential velocities at both sides of the fictitious Kutta-point which is impossible.

To study these effects for smooth round trailing edges, some numerical experiments on a circular cylinder have been performed initiated by South and Salas[16] who found similar results. The results shown in Fig. 3-5 have been achieved in a 34x32 O-mesh for a half-cylinder using the four stage two level scheme.

Fig. 3 portrayes nicely the results for $M_\infty = 0.20$ in pressure distribution solving the full potential equation and the Euler equations. Both solutions are fully converged to a residual of 10^{-12} and both agree completely. For $M_\infty = 0.50$ Fig. 4 shows quite different results. While the highly converged full

potential solutions gives a very strong shock and stagnation is reached with the corrects static pressure and q = 0 at the rear stagnation point. The Euler solutions indicates only minor differences at the forward part of the cylinder, shock position as well as pressure alread and behind the shock, however, differ quite a lot from the full potential solution. Most surprisingly, starting from .75 < 2x/DL.80 the static pressure from the Euler solution is constant and almost equal to cp = 0. Fig. 5 clarifies the results by presenting the direction of the local velocity vectors (length is scaled to the cell dimension!). The flow separates from the smooth surfaces and forms a recirculating "dead air"-region with very small velocities ($q \leq .01\ U_\infty$). It is interesting that the well known phenomena of nearly constant pressure in such a dead air region is computed by the present method without specifying anything specifically about this region. Although inviscid separation sounds strange for the first moment, it can be proven to be correct. The reason for this separation is total pressure loss by a shock rather than a boundary layer, however the consequences are similar since the flow due to the total pressure loss does not have enough kinetic energy to stagnate at the rear stagnation point. A possible potential flow model for this flow would be one containing free line vortices due to Crocco's law in addition to the doubled and parallel flow. However, it should be noted, that this separation point can be found to be always behind the one known from viscous flow analysis. It can be seen as a limit for $Re \to \infty$ in compressible flow if total pressure losses are apparent. This production of a vortex behind the cylinder can be also explained by other studies done on flow angularity. If a rotational onset flow has to pass a curved streamtube it is well known that under certain circumstances vortices with an axis normal to the flow can occur.

Since these examples indicate the basis capabilities of inviscid flow computations with the full Euler equations, the treatment of wakes in three-dimensional flow will only be mentioned briefly. All Kutta-conditions pertinent to the problem in consideration will show up automatically. Since the method is written in full conservation form, also discontinuities like shocks and wakes are captured properly. As known from supersonic flow studies, the accuracy can be improved by mesh alignment, which recommends to use a C-type mesh for wings since this will allow easily for wake-alignment.

VII. Results

The efficiency and accuracy of the Euler solver has been confirmed by numerical experiments. Some typical results are presented here. One nonlifting result is shown in Fig. 6 for the NACA 0012 airfoil at M=0.85. In a 64x32 O-Mesh for the half-plane the highly converged full potential solution using MAD and the Euler solution show 8% chord difference in shock position , the pressure jump is smaller as expected from the Rankine-Hugoniot condition, and the trailing edge pressure is reduced due to the total pressure loss. This Euler result used the full potential solution as initial solution and cp was converged after 300 cycles with a Courant number of 2 . Typical convergence characteristics for a similar case starting from scratch are depicted on Fig. 7 . Convergence behaviour is very smooth. Fig.8 shows corresponding results for a supersonic free stream Mach number , demonstrating the flexibility of the present method.

Fig.9 portrayes the comparison for lifting flow over the NACA 0012 airfoil using a 128x32 O-Mesh. Again, the full potential MAD-solution has been used as starting solution for the Euler solver. 500 Euler cycles with CFL=2 gave the converged solution. This time, not only the shock strength and position are different, but the complete pressure distribution. Lift and drag and moment coefficients deviate largly. Trailing edge pressure again is slightly reduced. The difference in lift can be explained as effect coming from the trailing edge Euler solution which does not need any explicit Kutta condition.Since there exists a total pressure loss on the upper surface, the flow is leaving the lower surface smoothly which corresponds to a small flap deflected upwards in potential flow. It should be mentioned that the Euler solver gave the same converged solution if the nonlifting full potential solution for this angle of attack was used having a flow around the trailing edge.

Further lifting results are not given in the present paper, since the next section will deal with airfoil results viscous effects included.

The experimental data of Cook, McDonald, and Firmin[17] include surface pressure and boundary-layer information for transonic flow about the RAE 2822 airfoil. Two sets of experimental data, denoted as Cases 6 and 9 in Ref. 17, are considered. Unfortunately these data, as all available transonic airfoil data, are not interference free. The values of Mach number and angle of attack corresponding to experimental (wind tunnel) conditions were

Case 6	Case 9
$M_\infty = 0.725$	$M_\infty = 0.730$
$\alpha = 2.92^0$	$\alpha = 3.19^0$

and the corrected Mach number and angle of attack values used for the present inviscid and viscid-inviscid interaction calculations were

Case 6	Case 9
$M_{\infty,corr} = 0.729$	$M_{\infty,corr} = 0.734$
$\alpha_{corr} = 2.44^0$	$\alpha_{corr} = 2.67^0$

The Reynolds number based on chord was 6.5×10^6 for both cases.

Comparisons of calculated and measured surface pressure data are given in Figs.10 and 11. The Mach number correction of 0.004 was that used by Lock[4] to obtain agreement between calculated and measured lower surface pressure distributions using a potential flow code for the inviscid flow. However, note in Figs.10 and 11 that the lower surface agreement obtained here using this Mach number correction is not good. The corrected angle of attacks were determined by the information provided by Cook, McDonald, and Firmin[17]. The calculated shock location using the corrected angle of attack is close to the experimental shock location for Case 9 in Fig.11, but the calculated shock location for Case 6 in Fig. 10 is about 3 percent chord forward of the experimental shock location. Adjustments in Mach number and angle of attack to match surface pressure distributions and hence lift coefficients were not made.

Comparisons of calculated and measured boundary-layer data are given in Figs.12-14. The calculated boundary-layer displacement thickness (δ^*/c) and momentum thickness (θ/c) distributions are slightly above the experimental data over the aft portion of the airfoil for Case 6 in Fig. 12 However, the calculated shock location is slightly forward of the experimental shock location as mentioned above, which may contribute to this difference. The calculated c_f, δ^*/c, and θ/c distributions for the stronger shock case in Fig. 13 are in good agreement with the experimental data, even in the shock-boundary-layer interaction region. A more detailed comparison of calculated and measured data throughout the shock region and at the trailing edge is given in Fig. 14 by boundary-layer velocity profile comparisons. The agreement between calculated and measured data in Fig. 14 is considered good. Calculated distributions of the source velocity $(\rho v)_n$, are included in Figs. 12 and 13. This term becomes significant in, and downstream, of the shock with large positive values occurring in the shock region and at the trailing edge. The source velocity becomes negative in the wake and reaches a minimum just aft of the trailing edge.

Finally, the capabilities of the present Euler method to solve the three-dimensional transonic or supersonic flow over wings and wing-body combinations are shown in Fig. 15 for the DFVLR-F4 wing-body transport configuration. This configuration exhibits a transonic wing design and was chosen to be a standard test case within GARTEur AG01. Since the three-dimensional wing-body code is fully operating in core, we are presently limited on the IBM 3031 to a 80x16x16 mesh. However, we are prepared to run the same configuration on a CRAY-1 using at least a 120x24x24 mesh which we feel to be sufficient for geometry and flow resolution. The Euler solution was obtained using a finite volume SLOR solution in the same mesh as initial solution. The FPE-solution was converged up to a residual of 10^{-4}. The Euler solution did converge after 300 cycles with CFL=2 and further 800 cycles did not change the solution any more. It is interesting to note that in the same mesh the Euler solution can resolve details better since velocities and pressures are direct variables while in the potential solution the velocities and ergo pressure result from numerical differentiation. In comparison with the experimental data, both, the FPE and the Euler solution seem to need a correction in Mach number to match the ex-

perimental data on the lower surface. The upper surface, however, is in much better agreement for the Euler solution and would even improve due to the expected Mach number correction. The differences have not been explored completely yet, but they seem to be mainly due to the better Kutta and wake treatment in the Euler solution.

VIII. CONCLUSIONS

The objectives of the present paper were to develop an efficient and accurate Euler solver to compute transonic and supersonic flow over two- and three-dimensional configurations. Since the same meshes were used in the Euler solver as for well established finite volume full potential solvers, the main differences between Euler and fully conservative FPE solutions could be demonstrated. The most important information has been that Euler solvers do not need any explicit Kutta condition to be unique neither in two- nor in three-dimensional flow. Even on smooth surfaces separation can occur in inviscid compressible flow caused by total pressure loss due to a shock. these effects help explaining the a priori unexpected differences between lifting Euler and full potential solutions. For viscous flow the Euler equations solver has been successfully coupled with an inverse boundary layer method. In comparison with experimental data, the wind tunnel corrections in Mach number and angle of attack as suggested by users of full potential solvers[4,6] does not result in total agreement if the Euler equations are being solved. High quality interference free experimental data are needed to verify methods like the present in detail. Unfortunately such data are evidently not available.

Computer times of the present Euler solver are 2ms per volume and cycle on the IBM 3031 computer. Corresponding times on the CRAY-1 computer were .04 ms. The CYBER 203 requires twice that much time.

IX. References

1 Jameson, A., Caughey, D.A.:
A Finite Volume Method for Transonic Potential Flow Calculations.
AIAA Paper 77-635, 1977

2 Boppe, C.W.:
Towards Complete Configurations Using an Embedded Grid Approach
NASA-CR 3030, July 1980

3 Schmidt, W.:
Aerodynamic Subsonic/Transonic Aircraft Design Studies by Numerical Methods.
AGARD CP 285, Paper 9, 1980

4 Lock, R.L.:
A Review of Methods for Predicting Viscous Effects on Aerofoils and Wings at Transonic Speeds.
AGARD-CPP-291, 1980

5 Deiwert, G.S.:
Recent Computation of Viscous Effects in Transonic Flow.
Lecture Notes in Physics No. 56, pp. 159-164, 1976 Springer

6 Melnik, R.E.:
Turbulent Interactions on Airfoils at Transonic Speeds - Recent Developments.
AGARD-CPP-291, 1980

7 Longo, J., Jameson, A., Schmidt, W.:
DOFOIL - A Viscous Analysis Program for Transonic Airfoil Flow.
Dornier FB 81, May 1981

8 van der Kolk, J.Th., Slooff, J.W.:
A Comparison of Computational Results for Transonic Flow Around the ONERA-M6 WING
NLR-REPORT prepared for GARTEur, AG (AD) 01, 1981

9 Mac Cormack, R.W., Warning, R.F.:
Survey of Computational Methods for Three-Dimensional Supersonic Inviscid Flows with Shocks.

Advances in Numerical Fluid Dynamics, AGARD LS 64, 1973

10 Jameson, A., Schmidt, W., Turkel, E.: Numerical Solutions of the Euler Equations by Finite Volume Methods Using Runge Kutta Time Stepping Schemes. AIAA-Paper 1259, June 1981

11 Catherall, D., Mangler, K.W.: The Integration of the Two-Dimensional Laminar Boundary Layer Equations Past the Point of Vanishing Skin Friction. Journal of Fluid Mechanics, Vol. 26, Part 1, pp 163-183, 1966

12 Whitfield, D.L., Swafford, T.W., Jacocks, J.L.: Calculation of Turbulent Boundary Layers with Separation, Reattachment, and Viscous-Inviscid Interaction. AIAA Paper 80-1439, July 1980

13 Carter, J.E.: A New Boundary Layer Inviscid Iteration Technique for Separated Flow. AIAA-Paper 79-1450, July 1979

14 Lighthill, M.J.: On Displacement Thickness Journal of Fluid Mechanics, Vol. 4, Part 4, pp 383-392, 1958

15 Yu, N.J.: Grid Generation and Transonic Flow Calculations for Three-Dimensional Configurations. AIAA-Paper 80-1391, July 1980

16 South, J.C., Salas, M.: Private Communication, Sept. 1980

17 Cook, P.H., McDonald, M.A., Firmin, M.C.P.: Aerofoil RAE 2822 Pressure Distributions and Boundary Layer Measurements . AGARD-AR-138, 1979

18 Slooff, J.W. F-4 Wing. Results of Pressure Measurements (NLR-TEST) for the Theoretical Test Cases. NLR note AT/2789 , Oct 1980

X . FIGURES

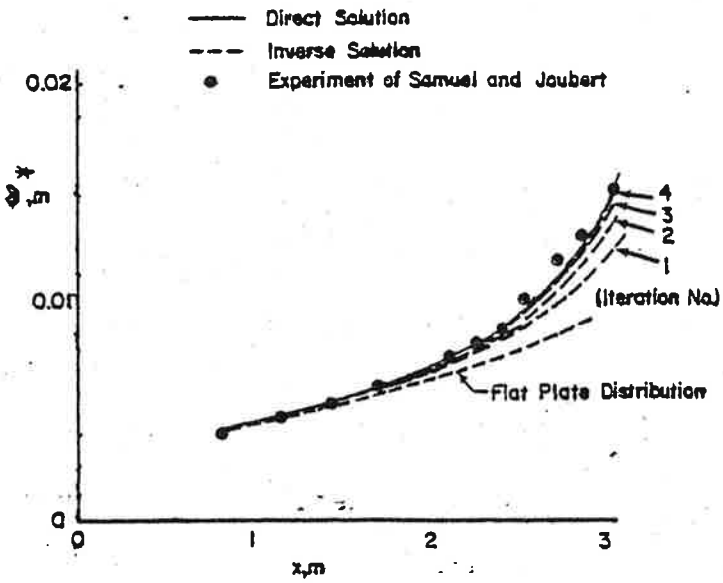

Fig. 1: Direct and Invers Boundary Layer Calculations of an Increasingly Adverse Pressure Gradient Flow.

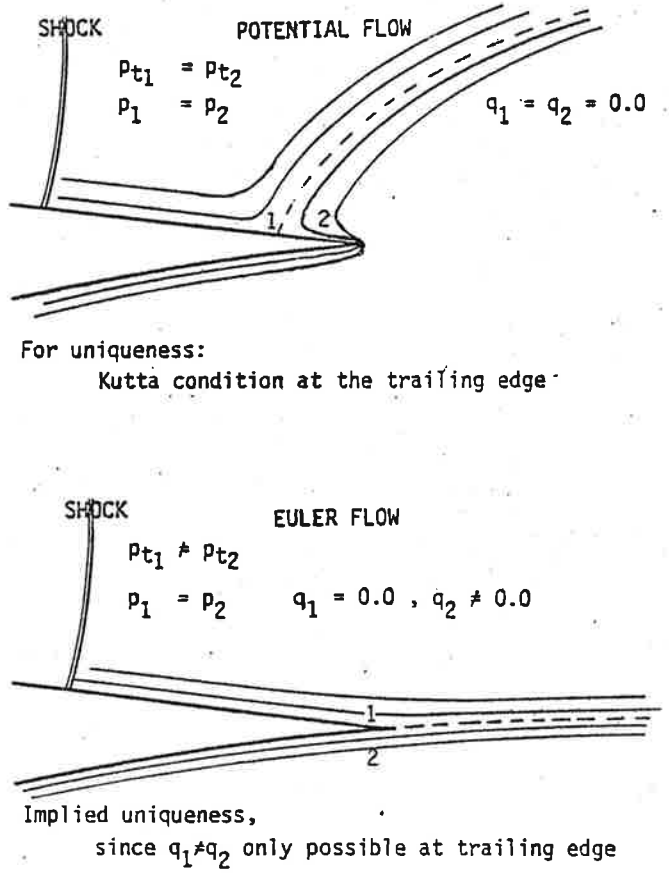

Fig. 2: Trailing Edge Flow for Rotational Flow

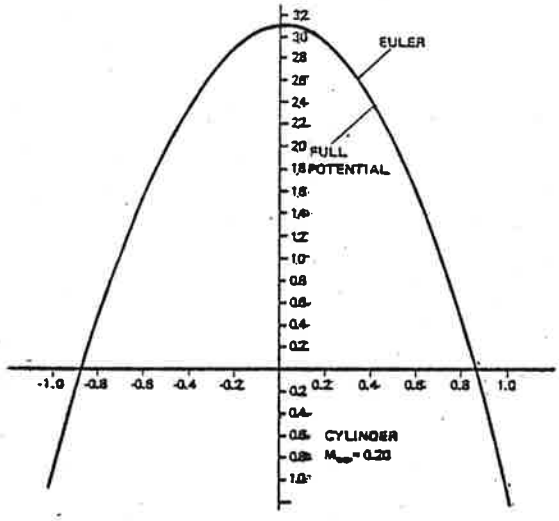

Fig. 3: Flow Around a Circular Cylinder M=0.2

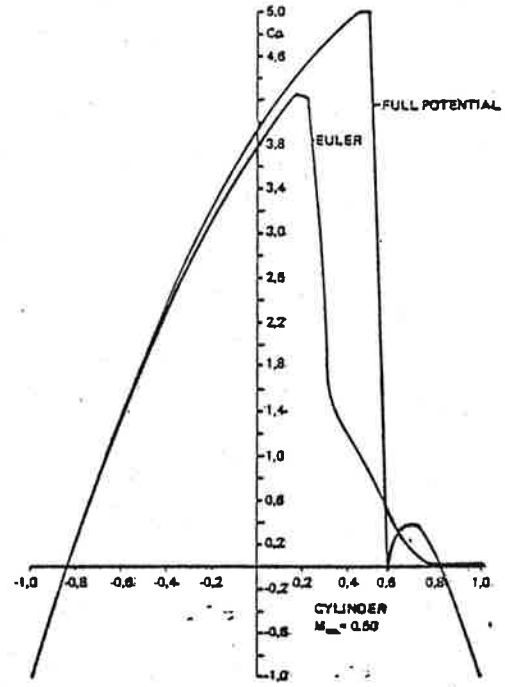

Fig. 4: Flow Around a Circular Cylinder M=0.5

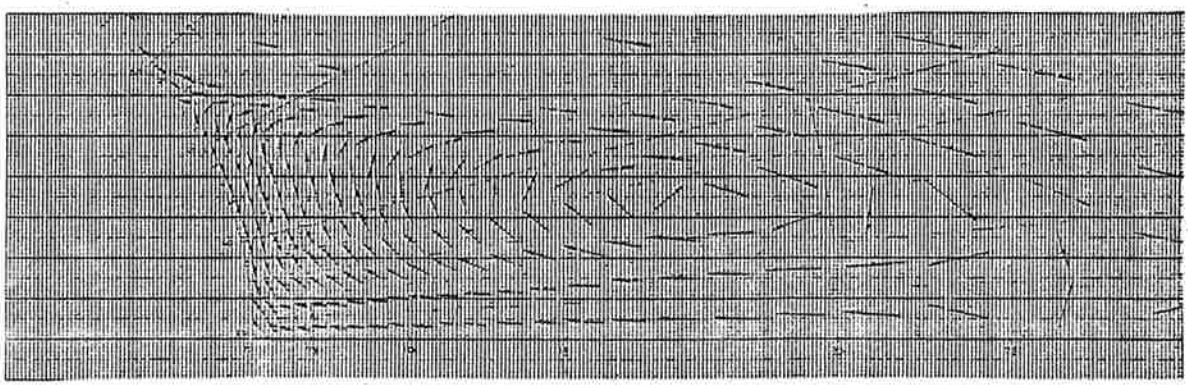

Fig. 5: Local Flow Velocity Direction Plot Behind a Circular Cylinder M=0.5

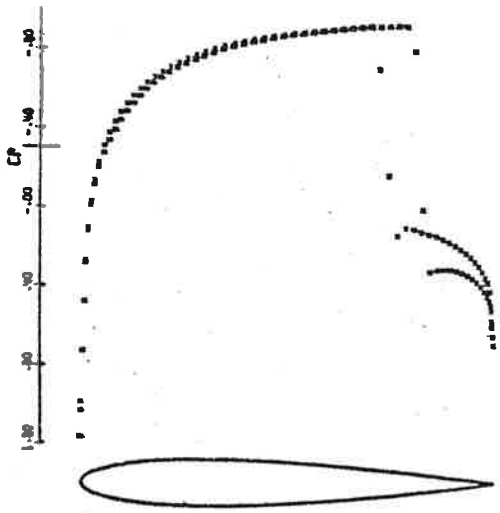

Fig. 6: Nonlifting Flow Over NACA 0012 at M=0.85

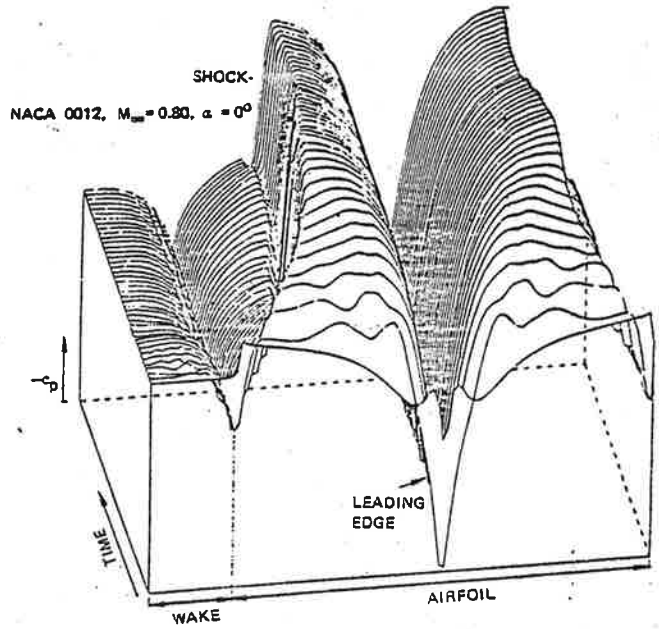

Fig. 7: Convergence Characteristics for Euler solution Starting from Scratch

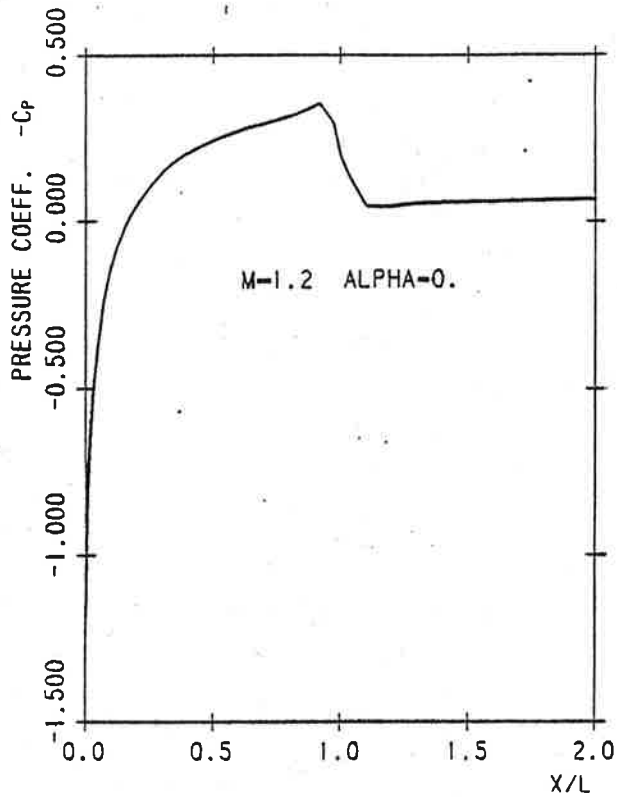

Fig. 8: Nonlifting Flow over NACA 0012 at M=1.2

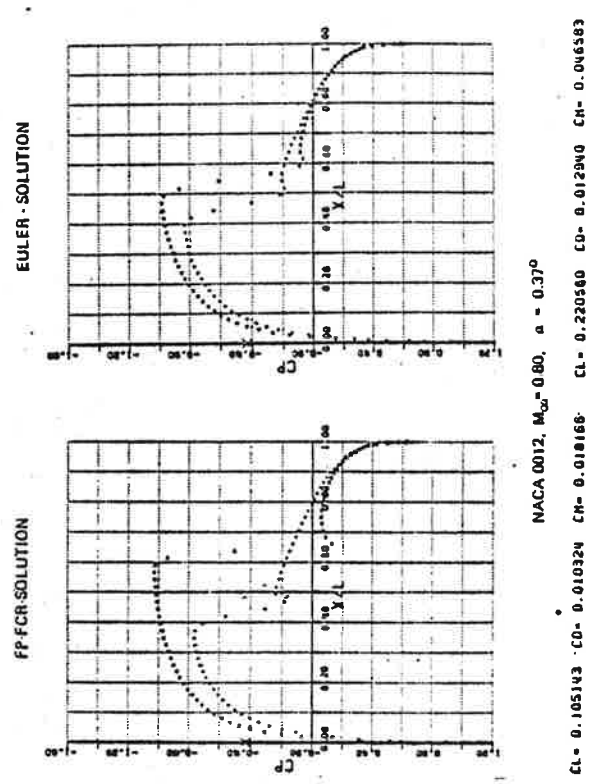

Fig. 9: Comparison of Lifting Flow Over NACA 0012 Between Euler and FPE

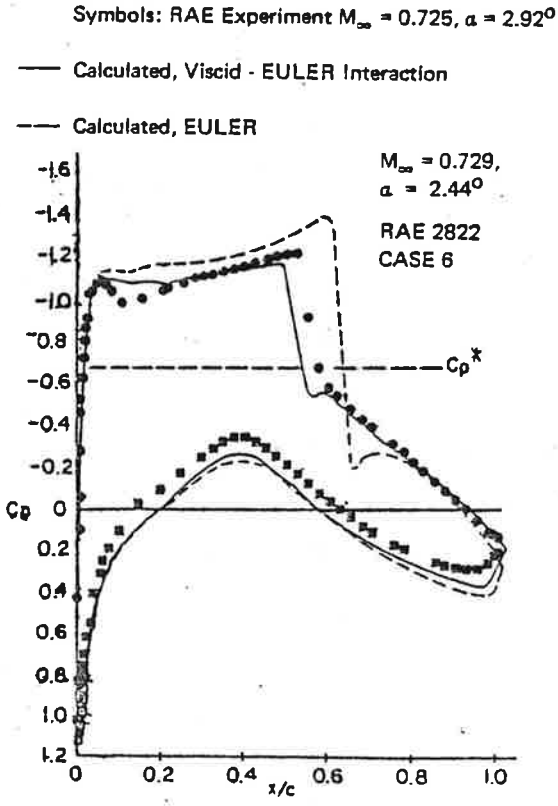

Fig. 10: Surface Pressures on the RAE 2822 Airfoil for Case 6

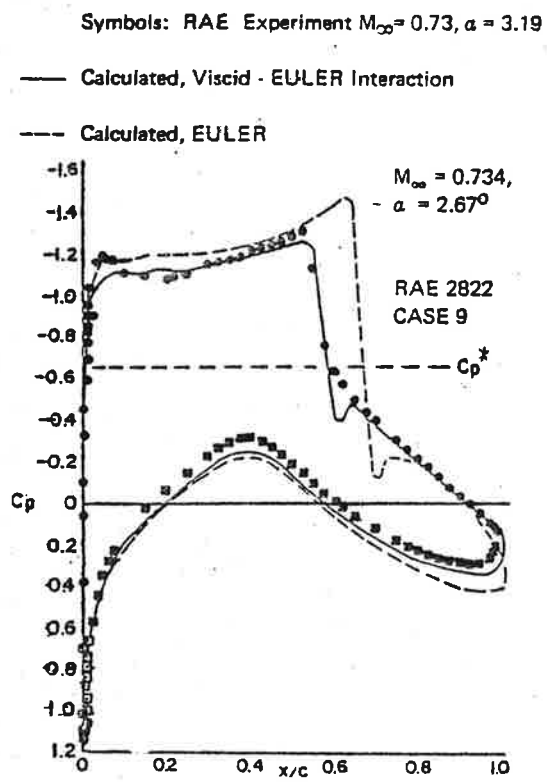

Fig. 11: Surface Pressures on the RAE 2822 Airfoil for Case 9

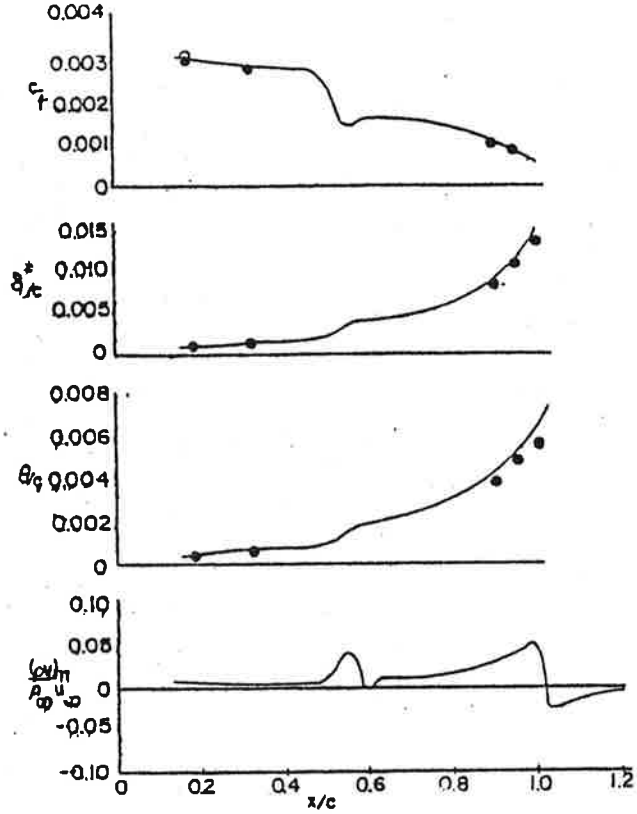

Fig. 12: Boundary Layer Data on the RAE 2822 Airfoil Upper surface for Case 6

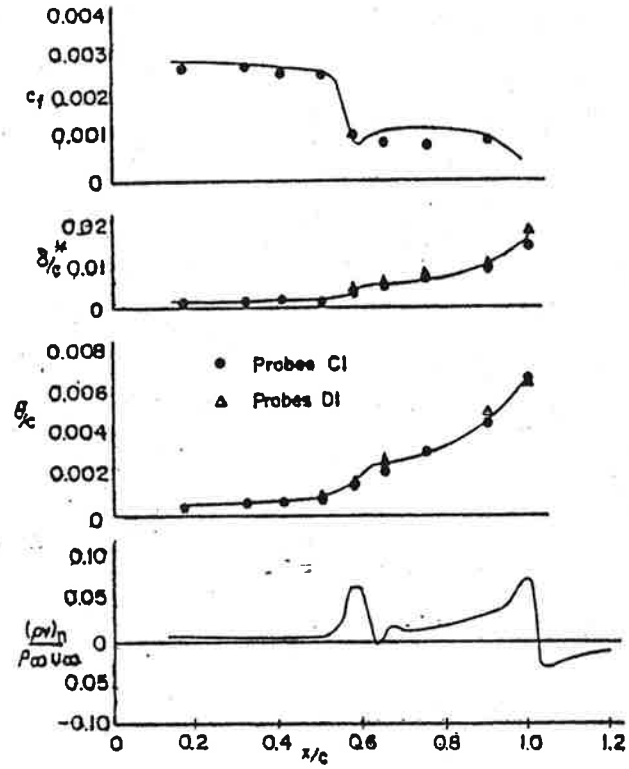

Fig. 13: Boundary Layer Data on the RAE 2822 Airfoil Upper Surface for Case 9

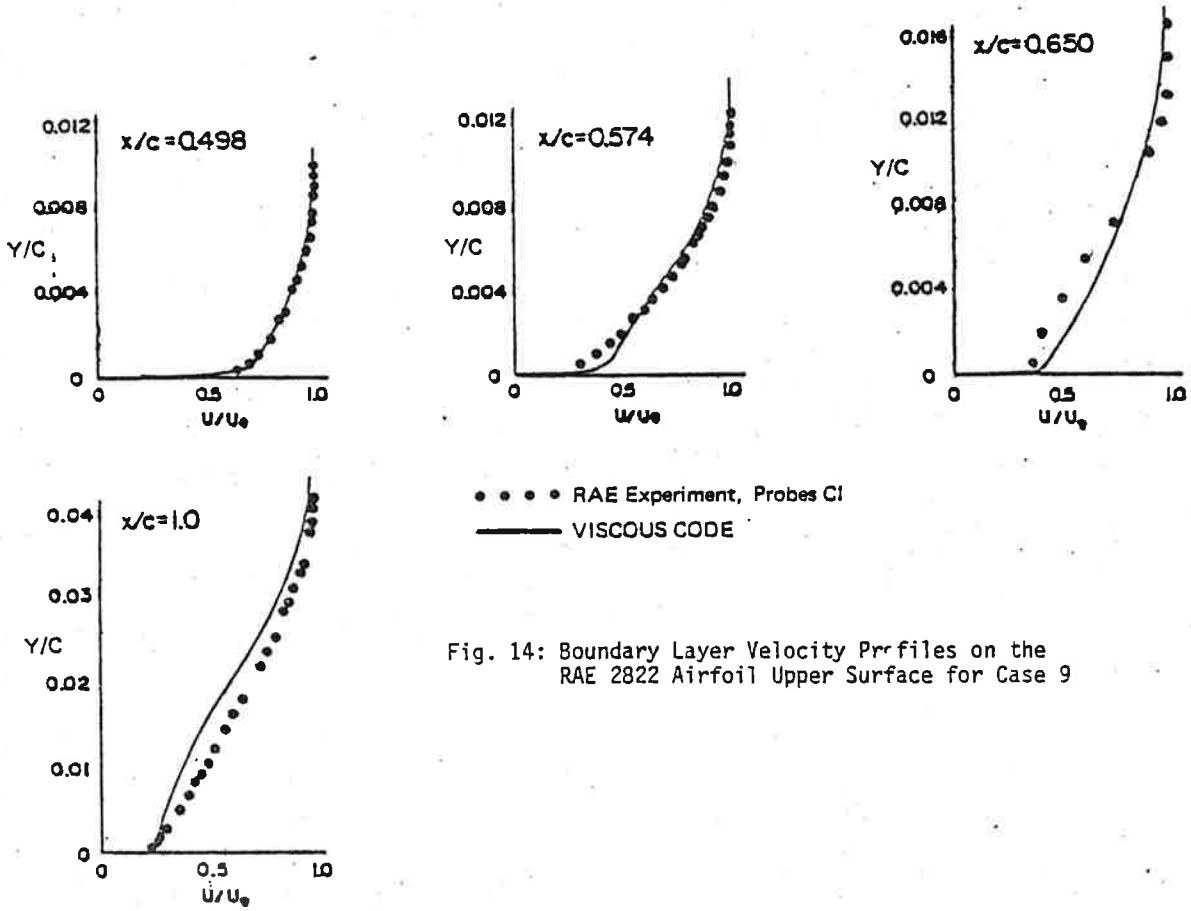

Fig. 14: Boundary Layer Velocity Profiles on the RAE 2822 Airfoil Upper Surface for Case 9

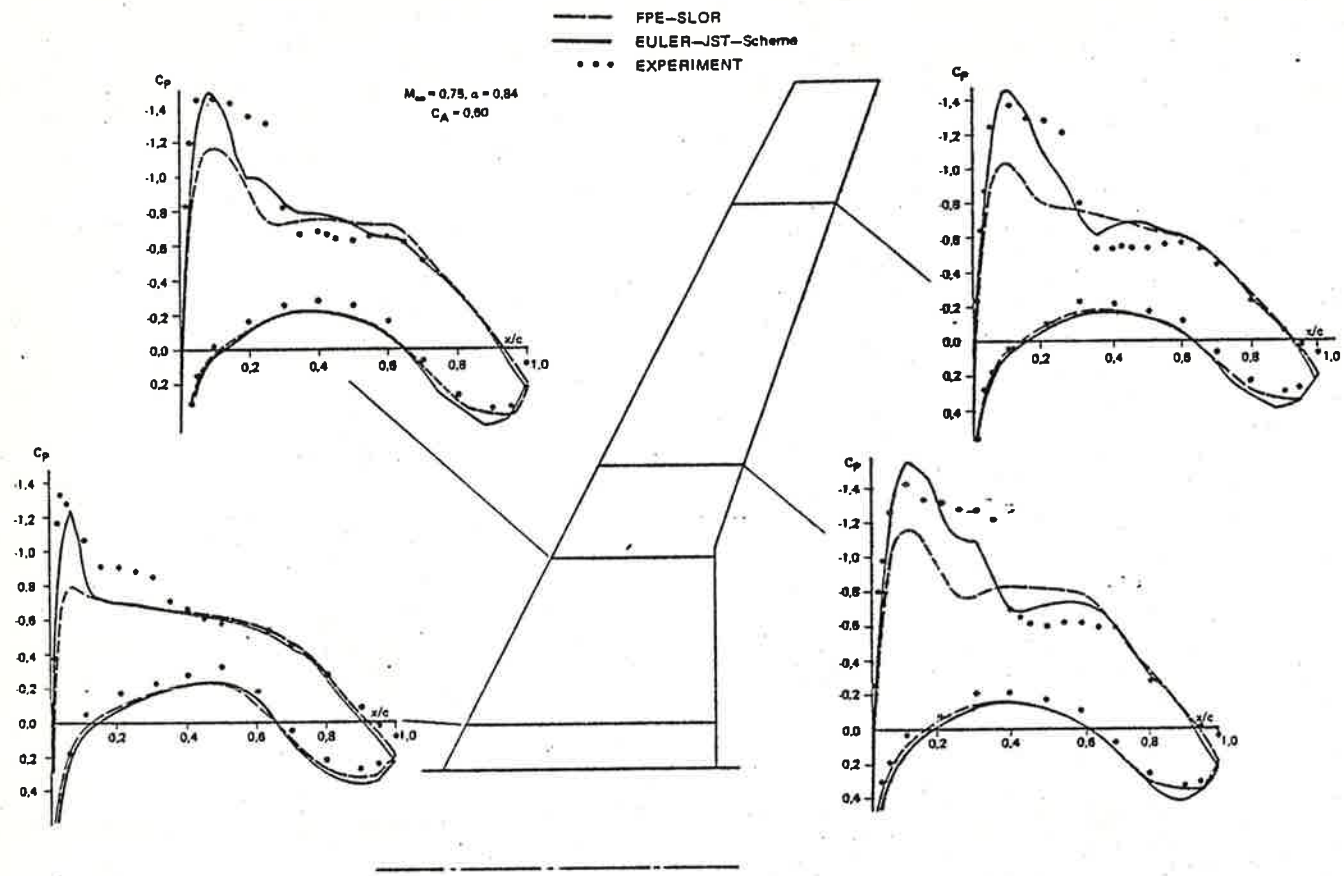

Fig. 15: Comparison of Euler and Full Potential Solution Against Experimental Data for the DFVLR-F4 Wing-Body Combination.